A&A 490, 265–277 (2008)
DOI: 10.1051/0004-6361:200810169

Astronomy & Astrophysics

The core helium flash revisited

I. One and two-dimensional hydrodynamic simulations

M. Mocák, E. Müller, A. Weiss, and K. Kifonidis

Max-Planck-Institut für Astrophysik, Postfach 1312, 85741 Garching, Germany
e-mail: mmocak@mpa-garching.mpg.de

Received 9 May 2008 / Accepted 5 August 2008

ABSTRACT

Context. We investigate the hydrodynamics of the core helium flash close to its peak. Past research concerned with the dynamics of this event is inconclusive. However, the most recent multidimensional hydrodynamic studies suggest a quiescent behavior and seem to rule out an explosive scenario.
Aims. Depending on initial conditions, turbulence models, grid resolution, and dimensionality of the simulation, previous work indicated that the core helium flash could lead either to the disruption of a low-mass star or to a quiescent quasi-hydrostatic evolution. We attempt to clarify this issue by simulating the evolution with advanced numerical methods and detailed microphysics.
Methods. Assuming spherical or axial symmetry, we simulate the evolution of the helium core of a 1.25 $M_\odot$ star with a metallicity $Z = 0.02$ during the core helium flash at its peak with a grid-based hydrodynamical code.
Results. We find that the core helium flash neither rips the star apart, nor significantly alters its structure, since convection plays a crucial role in keeping the star in hydrostatic equilibrium. In addition, our simulations indicate the presence of overshooting, which implies new predictions concerning mixing of chemical species in red giants.

Key words. stars: evolution – hydrodynamics – convection – stars: interiors

1. Introduction

In stars of mass $0.7\ M_\odot \leq M \leq 2.2\ M_\odot$, the onset of helium burning constitutes a major event – the core helium flash. The pre-flash stellar core contains a white dwarf-like degenerate structure with a central density of about 10^6 g cm^{-3}, and an off-center temperature maximum resulting from plasma- and photo-neutrino cooling. When helium burning commences in this degenerate core, the liberated nuclear energy cannot be used to expand and cool the layers close to the temperature maximum. Instead it causes further heating and a strong increase in the nuclear energy release. Only when convection sets in can part of the excess energy be transported away from the burning regions, inhibiting a thermonuclear explosion. By the end of the flash, the core has expanded to densities of the order of 10^4 g cm^{-3}, helium burning continues quiescently in the center, and the star has settled onto the horizontal branch. While standard stellar evolution calculations have been successful in reproducing observations of stars on the main sequence and the red giant branch (RGB), we recognize several discrepancies concerning the post-flash phases. In particular, we recall the lack of understanding about the horizontal-branch morphology, low-luminosity carbon stars, and hydrogen-deficient stars. Since all of these (and other) problems appear after the RGB phase, it is plausible to suspect that the helium flash may be treated incorrectly in standard (hydrostatic) stellar evolution calculations.

The conceptual problems associated with the helium core flash arise from the extremely short timescales involved in the event. While the pre-flash evolution proceeds on a nuclear timescale of $\sim 10^8$ yrs, typical e-folding times for the energy release from helium burning can become as short as hours at the peak of the flash. These short times are comparable to convective turnover times, i.e. the common assumptions used for the treatment of convection in stellar evolution codes (instantaneous mixing, time-independence) are no longer valid. In addition, the assumption of hydrostatic equilibrium no longer needs to be fulfilled. Early attempts to avoid these assumptions by modeling one-dimensional hydrodynamic flow (Edwards 1969; Zimmermann 1970; Villere 1976; Wickett 1977) remained inconclusive. The results ranged from a confirmation of the standard picture to a complete disruption of the star.

Cole & Deupree (1980, 1981) performed a two-dimensional hydrodynamic study of the core helium flash. However, their study was limited by the computational resources available at that time to a rather coarse computational grid (23×4 zones), a diffusive first-order difference scheme (weighted donor cell), and a short time evolution (10^5 s compared to the duration of the core helium flash of 10^{11} s from the onset of convection). At the radius of the off-center temperature maximum, they observed a series of thermonuclear runaways where heat transport by convection and conduction was sufficiently efficient to limit the rise in temperature. Each runaway modified the convective flow pattern and generated some inward transport of heat across the off-center temperature inversion. During the simulation, the time interval between runaways continuously shortened, and the maximum temperature steadily increased until it eventually exceeded 10^9 K.

Deupree & Cole (1983) and (Deupree 1984a,b) confirmed these findings using two-dimensional models with an improved angular resolution (6° instead of 20°), and three-dimensional

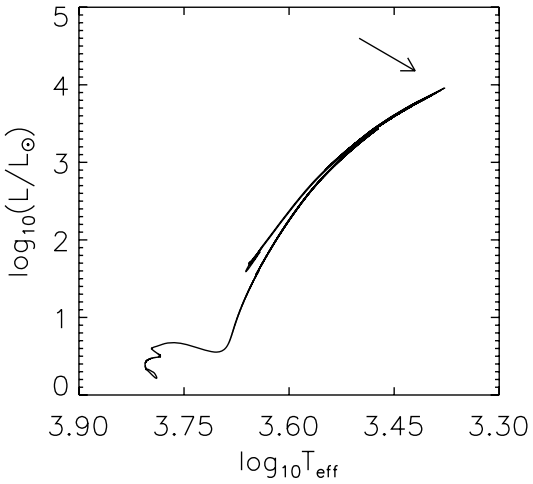

Fig. 1. Theoretical evolutionary track of a 1.25 $M_\odot$ star with a metallicity $Z = 0.02$ in the H-R diagram. The core helium flash begins at the the tip of the red giant branch indicated by the arrow.

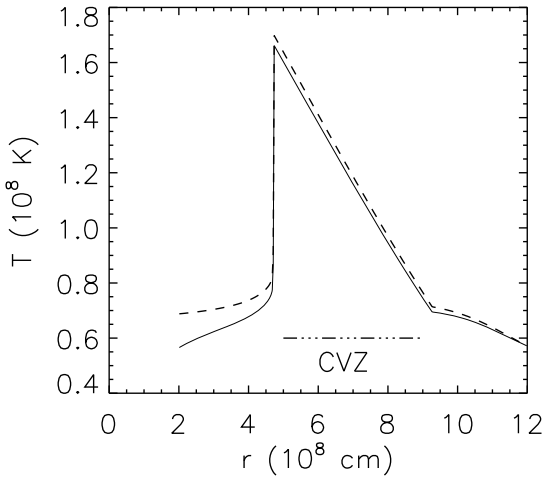

Fig. 2. Temperature distribution as a function of radius. The dashed line gives the distribution obtained from stellar evolutionary calculations, while the solid line shows the mapped and stabilized distribution used as initial condition in the hydrodynamic simulations. CVZ marks the convection zone.

simulations (with 8 × 8 angular zones in a 80° × 80° cone, i.e. 10° angular resolution). Cole et al. (1985) performed stellar evolution calculations of the core helium flash using a model for convective overshooting based on these hydrodynamic simulations. They found that the evolution of the core helium flash was unchanged except for the last week prior to its peak. Furthermore, the possibility of the mixing of core material into the hydrogen shell was suggested by numerical experiments where point source explosions were enforced (Deupree 1984b, 1986; Deupree & Wallace 1987). These results raised the hope that some problems concerning abundance anomalies and mass loss could be solved by understanding the core helium flash.

The results of the hydrodynamic simulations, though varying in details, indicated a dynamic flash that could disrupt the star (Deupree 1984a) or at least lead to a significant loss of the envelope (Cole & Deupree 1981). The simulations were critized by Iben & Renzini (1984) and Fujimoto et al. (1990) because (i) the radial grid was too coarse; (ii) the gravitational potential was "frozen in" (i.e. time-independent); and (iii) because a "closed" outer boundary was used. The last two assumptions tend to underestimate the expansion of the core, and hence overestimate the violence of the flash.

Since the work of Deupree the computational capabilities have grown tremendously and methods to simulate hydrodynamic flow have improved considerably. The limitations of early studies concerning grid resolution and numerical treatment, the main points of critique, can therefore be reduced considerably. At the same time, we still do not know the extent or circumstances (stellar mass and composition) in which hydrodynamic core helium flash evolution differ from canonical stellar evolution calculations. Therefore, it appears necessary to have a new and fresh look into the dynamics of the core helium flash. Deupree (1996) re-examined the problem, already more than a decade ago, concluding that the flash does not lead to any hydrodynamic event. Quiescent behaviour of the core helium flash is also favored by three-dimensional simulations done by Dearborn et al. (2006) and Lattanzio et al. (2006), in which the energy transport due to convection, heat conduction, and radiation appears able to transport most of the energy generated during the flash quiescently from the stellar interior to the outer stellar layers, implying no hydrodynamic event, and hence a quasi-hydrostatic evolution.

We present a completely independent investigation of the core helium flash by means of one-dimensional and two-dimensional hydrodynamic simulations using state-of-the-art numerical techniques, a detailed equation of state, and a time-dependent gravitational potential. The hydrodynamic calculations cover about 8 h of the evolution close to the peak of the core helium flash. We note that the present investigation was instigated by a similar, technically obsolete study performed by Kurt Achatz (Achatz 1995) in the context of his diploma thesis. The results of this latter study have unfortunately never been published.

The paper is organized as follows. In Sect. 2, we discuss briefly the stellar input model for the simulations along with some results from hydrostatic core helium flash calculations. In Sect. 3, the hydrodynamics code and the numerical methods are introduced, while the results of our one and two-dimensional (1D and 2D, respectively) hydrodynamic runs are presented in Sects. 4 and 5, respectively. Finally, our conclusions are given in Sect. 6.

2. Initial stellar models and hydrostatic calculations

Table 1 summarizes some properties of our initial model, which was obtained from stellar evolutionary calculations with the "Garstec" code (Weiss & Schlattl 2000, 2007). It corresponds to a star with a mass of 1.25 $M_\odot$ and a metallicity $Z = 0.02$ at the peak of the core helium flash ($L_{\rm He} \sim 10^9\ L_\odot$), computed with the hydrostatic stellar evolution code. During this violent episode, the star is located at the tip of the red giant branch in the H-R diagram (Fig. 1), hence being a red giant consisting of a small central helium core with a radius $r \sim 1.9 \times 10^9$ cm, surrounded by a hydrogen burning shell and a huge convective envelope with a radius $r \sim 10^{13}$ cm. Figure 2 shows the temperature distribution inside the helium core, which is characterized by an off-center temperature maximum $T_{\rm max}$, from where the temperature steeply drops towards smaller radii and follows a super-adiabatic gradient towards larger radii (convection zone). The radius $r_{\rm max}$ of the temperature maximum coincides with the bottom of the convection zone. The almost discontinuous temperature stratification near $T_{\rm max}$ (temperature inversion), where the temperature rises from 7×10^7 K to 1.7×10^8 K, results

Table 1. Some properties of the initial model: total mass M, stellar population, metal content Z, mass $M_{\rm He}$ and radius $R_{\rm He}$ of the helium core ($X(^4{\rm He}) > 0.98$), nuclear energy production in the helium core $L_{\rm He}$, maximum temperature of the star $T_{\rm max}$, and radius $r_{\rm max}$ and density $\rho_{\rm max}$ at the temperature maximum.

Model	M [$M_\odot$]	Pop.	Z	$M_{\rm He}$ [$M_\odot$]	$R_{\rm He}$ [10^9 cm]	$L_{\rm He}$ [10^9 $L_\odot$]	$T_{\rm max}$ [10^8 K]	$r_{\rm max}$ [10^8 cm]	$\rho_{\rm max}$ [10^5 g cm^{-3}]
M	1.25	I	0.02	0.47	1.91	1.03	1.70	4.71	3.44

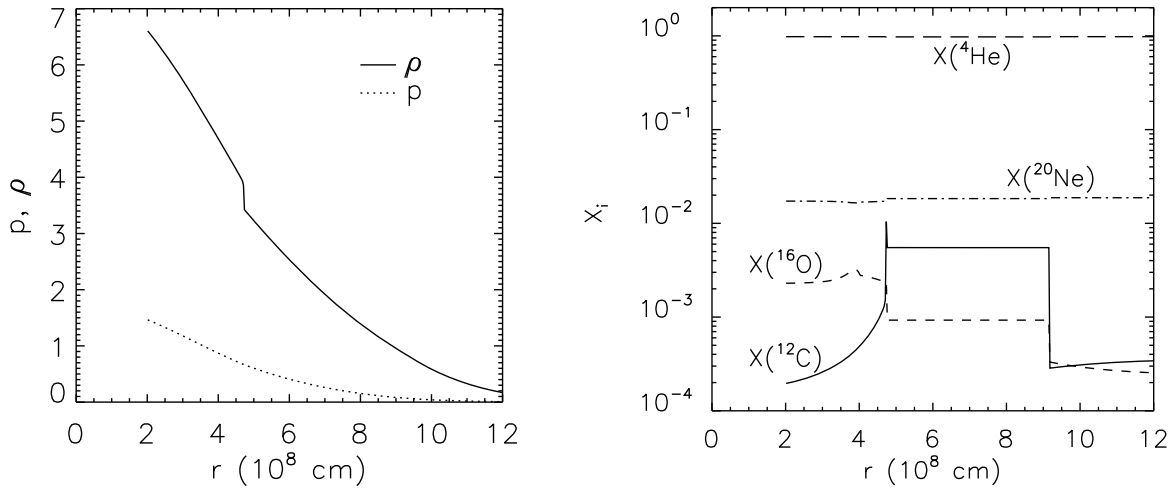

Fig. 3. *Left panel*: pressure (in 10^{22} dyn cm^{-2}) and density (in 10^5 g cm^{-3}) distribution of the mapped and stabilized initial model. The pressure and density distribution of the original stellar evolution model cannot be distinguished from the corresponding profiles of the stabilized model on this scale. *Right panel*: chemical composition of the initial model.

from an interplay between neutrino cooling and heating by nuclear burning. Figure 3 shows the density and pressure stratification of the model. One recognizes that the temperature inversion is correlated with a drop in density. A detailed view reveals that the steep increase in temperature corresponds to a decrease in the density by 11%, an increase in the ion pressure by 70%, and a drop in the electron pressure by 9%, respectively. Even at the peak of the core helium flash, the helium core is still strongly degenerate: compared with the electron pressure, the ion pressure is lower by a factor of 6, while the radiation pressure is smaller by almost 3 orders of magnitude.

The stellar model contains the chemical species ^{1}H, ^{3}He, ^{4}He, ^{12}C, ^{13}C, ^{14}N, ^{15}N, ^{16}O, ^{17}O, ^{24}Mg, and ^{28}Si. However, we are not interested in the detailed chemical evolution of the star. It is therefore unnecessary to consider all of these species in our hydrodynamic simulations, since the triple-α reaction dominates the energy production rate during the core helium flash. In our hydrodynamic simulations, we therefore adopt only the abundances of ^{4}He, ^{12}C, and ^{16}O. The remaining composition is assumed to be adequately represented by a gas with a mean molecular weight equal to that of ^{20}Ne (Fig. 3). The apparent peak in ^{12}C abundance at the position of the temperature maximum results from a non-instantaneous treatment of convective mixing.

The stellar evolutionary model is one-dimensional, hydrostatic, and was computed on a Lagrangian grid of 2294 zones. Since only the helium core of the model (without its very central part; see Sect. 3.6) is of interest to us, we consider only the initial data for 2×10^8 cm $\leq r \leq 1.2 \times 10^9$ cm, and interpolate all relevant quantities (e.g. density, temperature, composition) onto our Eulerian, lower resolution computational grid using polynomial interpolation (Press et al. 1992). Due to the interpolation errors and subtle differences in the input physics, the interpolated model is no longer in perfect hydrostatic equilibrium. To balance perfectly also the gravitational and pressure forces in the interpolated model, we use an iterative procedure in the first hydrodynamic timestep to minimize the numerical fluxes across zone boundaries. The entire process produces a small temperature decrease with respect to the temperature profile of the original model (Fig. 2). Depending on the radial resolution of the Eulerian grid, the differences do not exceed a few percent. The resulting changes in the density and pressure profiles are negligible due to the strong electron degeneracy of the gas. The main cause of the slight destabilization of the mapped initial stellar model is the use of different equations of state in both codes. The hydrodynamic code employs the equation of state by Timmes & Swesty (2000), whereas the "Garstec" code relies on the OPAL equation of state by Rogers et al. (1996). At a given density, temperature, and composition in the helium core during the flash, these equations of state provide pressure values that differ typically by 1%, the difference being most apparent in regions where the matter is highly degenerate.

Given that the maximum temperature in the helium core is $T \sim 1 \times 10^8$ K, the stellar model reaches a peak in nuclear energy production rate during the core helium flash within 10^4 yrs. The rate at which the nuclear energy production rises is highly non-linear. From the onset of the core helium flash at a helium luminosity of $L_{\rm He} \sim 10^1$ $L_\odot$, it takes almost 30 000 yrs to reach $L_{\rm He} \sim 10^4$ $L_\odot$, whereas it requires only 40 yrs to reach $L_{\rm He} \sim 10^{10}$. The first core helium flash is followed by four subsequent mini flashes (Fig. 4) identified as thermal pulses by Thomas (1967) until the degeneracy in the helium core is lifted

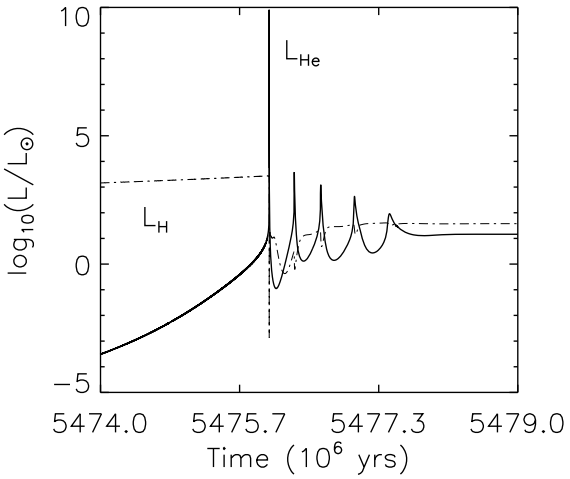

Fig. 4. Temporal evolution of the helium luminosity $L_{\rm He}$ (solid) versus the hydrogen luminosity $L_{\rm H}$ (dash-dotted) of model M during the core helium flash.

completely and the star settles down onto the horizontal branch quiescently burning helium in its core.

Since the computed model is a Pop I metal-rich star, it does not experience any hydrogen entrainment during the core helium flash (Fujimoto et al. 1990; Schlattl et al. 2001).

3. Input physics and numerics

3.1. Thermal transport

The energy flux density due to thermal transport is given by

$$f_{\rm cond} = -K_{\rm cond}\nabla T, \tag{1}$$

where $K_{\rm cond}$ is the total conductivity (erg K^{-1} cm^{-1} s^{-1}) and ∇T the temperature gradient.

In the helium core, which is partially degenerate, thermal transport due to both radiative diffusion and electron conduction is important, while heat transport by ions is negligible, i.e.

$$K_{\rm cond} = K_\gamma + K_{\rm e}. \tag{2}$$

The radiative conductivity is given by

$$K_\gamma = \frac{4ac}{3}\frac{T^3}{\kappa_\gamma \rho}, \tag{3}$$

where κ, a, and c are the Rosseland mean of the opacity, the radiation constant, and the speed of light, respectively. For the opacity, we use a formula defined by Iben (1975), which is based on the work of Cox & Stewart (1970a,b). It takes into account the radiative opacity due to Thomson scattering, free-free (Kramers opacity), bound-bound, and bound-free transitions.

For the thermal transport by electron conduction, we consider contributions due to electron-ion and electron-electron collisions (Yakovlev & Urpin 1980; Potekhin et al. 1997).

3.2. Neutrino emission

The evolutionary time covered by our hydrodynamic simulations is too short for neutrino cooling to be of importance. The neutrino losses computed from the analytic fits of Itoh et al. (1996) provide a cooling rate $\dot{\epsilon} < 10^2$ erg g^{-1} s^{-1}, or a corresponding decrease in the maximum temperature by $|\Delta T| < 10^{-1}$ K during the longest simulations that we performed. Hence, cooling by neutrinos was neglected.

3.3. Equation of state

The equation of state employed in our hydrodynamic code includes contributions due to radiation, ions, electrons, and positrons. The total pressure is therefore given by

$$P = P_\gamma + P_{\rm ion} + P_{\rm e} + P_{\rm p}, \tag{4}$$

where

$$P_\gamma = \frac{a}{3}T^4 \tag{5}$$

is the radiation pressure of a black body of temperature T, a is the universal radiation constant, and

$$P_{\rm ion} = \sum_i \Re\frac{\rho X_i}{A_i}T = \Re\rho T\sum_i Y_i \tag{6}$$

is the pressure of a non-relativistic Boltzmann gas of density ρ which consists of a set of ions of abundance $Y_i = X_i/A_i$ (where X_i and A_i are the mass fraction and the atomic mass number of species i, respectively). The pressure of an arbitrarily degenerate and relativistic electron-positron gas $P_{\rm e} + P_{\rm p}$ is based on table interpolation of the Helmholtz free energy (Timmes & Swesty 2000).

3.4. Nuclear burning

The energy generation rate by nuclear burning is given by

$$\dot{\varepsilon}_{\rm nuc} = \sum_i \frac{\Delta m_i c^2}{m_{\rm u}}\dot{Y}_i \tag{7}$$

where

$$\Delta m_i = M_i - A_i m_{\rm u}, \tag{8}$$

is the mass excess of a nucleus of mass M_i, and $m_{\rm u}$ is the atomic mass unit.

Abundance changes are described by a nuclear reaction network consisting of the four α-nuclei ^{4}He, ^{12}C, ^{16}O, and ^{20}Ne, coupled by seven reactions (including the triple-α reaction). We used the reaction rate library of Thielemann (private communication), which provides the product of the Avogadro number $N_{\rm A}$ and the velocity averaged cross section $\langle\sigma v\rangle$ in terms of the fit formula

$$N_{\rm A}\langle\sigma v\rangle = \sum_{l=1}^{n_l}\exp\Big[c_{1l} + c_{2l}T^{-1} + c_{3l}T^{-1/3} + c_{4l}T^{1/3} + c_{5l}T + c_{6l}T^{5/3} + c_{7l}\ln T\Big], \tag{9}$$

with rate dependent coefficients c_{il} ($1 \le i \le 7$). Up to three sets of coefficients (i.e. $1 \le n_l \le 3$) are used. The total reaction rate due to all one-body, two-body, and three-body interactions has the form (Müller 1998):

$$\dot{Y}_i = \sum_j c_i\lambda_j Y_j + \sum_{j,k} c_i(j,k)\rho N_{\rm A}\langle\sigma v\rangle_{j,k}Y_jY_k + \sum_{j,k,l} c_i(j,k,l)\rho^2 N_{\rm A}^2\langle\sigma v\rangle_{j,k,l}Y_jY_kY_l, \tag{10}$$

where the weight factors c_i inhibit multiple counts in the sums over the nuclei j, k, l. The following nuclear reactions were considered:

$$
\begin{array}{lllllllll}
\mathrm{He}^4 & + & \mathrm{C}^{12} & \rightarrow & \mathrm{O}^{16} & + & \gamma & & \\
\mathrm{He}^4 & + & \mathrm{O}^{16} & \rightarrow & \mathrm{Ne}^{20} & + & \gamma & & \\
\mathrm{O}^{16} & + & \gamma & \rightarrow & \mathrm{He}^4 & + & \mathrm{C}^{12} & & \\
\mathrm{Ne}^{20} & + & \gamma & \rightarrow & \mathrm{He}^4 & + & \mathrm{O}^{16} & & \\
\mathrm{C}^{12} & + & \mathrm{C}^{12} & \rightarrow & \mathrm{Ne}^{20} & + & \mathrm{He}^4 & & \\
\mathrm{He}^4 & + & \mathrm{He}^4 & + & \mathrm{He}^4 & \rightarrow & \mathrm{C}^{12} & + & \gamma \\
\mathrm{C}^{12} & + & \gamma & \rightarrow & \mathrm{He}^4 & + & \mathrm{He}^4 & + & \mathrm{He}^4.
\end{array}
$$

Mathematically, this produces a nuclear reaction network consisting of seven non-linear first-order differential equations of the form given by Eq. (10) and a temperature equation

$$\frac{\partial T}{\partial t} = \dot{\varepsilon}_{\mathrm{nuc}} \frac{\partial T}{\partial \varepsilon}, \tag{11}$$

where ε is the specific internal energy.

The effects of electron screening according to Dewitt et al. (1973) were included for the triple-α reaction rate, and in the weak screening regime only.

3.5. Evolutionary equations

The hydrodynamic and thermonuclear evolution of the core helium flash was computed by solving the governing set of fluid dynamic equations in spherical coordinates on an Eulerian grid. Using vector notation, these equations have the form,

$$\frac{\partial \boldsymbol{U}}{\partial t} + \nabla \boldsymbol{F} = \boldsymbol{S} \tag{12}$$

with the state vector $\boldsymbol{U}$

$$\boldsymbol{U} \equiv \begin{pmatrix} \rho \\ \rho \boldsymbol{v} \\ \rho e \\ \rho Y_i \end{pmatrix} \tag{13}$$

the flux vector $\boldsymbol{F}$

$$\boldsymbol{F} \equiv \begin{pmatrix} \rho \boldsymbol{v} \\ \rho \boldsymbol{v}\boldsymbol{v} \\ (\rho e + p)\boldsymbol{v} + f_{\mathrm{cond}} \\ \rho Y_i \boldsymbol{v} \end{pmatrix} \tag{14}$$

and the source vector $\boldsymbol{S}$

$$\boldsymbol{S} \equiv \begin{pmatrix} 0 \\ -\rho \nabla \Phi \\ -\rho \boldsymbol{v} \cdot \nabla \Phi + \rho \dot{\epsilon}_{\mathrm{nuc}} \\ \rho \dot{Y}_i \end{pmatrix} \tag{15}$$

with $i = 1, \ldots, N_{\mathrm{nuc}}$, where N_{nuc} is the number of nuclear species considered in the nuclear reaction network, and ρ, p, $\boldsymbol{v}$, and Φ are the density, pressure, velocity, and gravitational potential, respectively. The term f_{cond} describes energy transport by thermal conduction (see Sect. 3.1), and $\dot{\epsilon}_{\mathrm{nuc}}$ and the $\dot{Y}_i$ are the nuclear energy generation rate and the change in the mass fraction of species i due to nuclear reactions, respectively (see Sect. 3.4). The total energy density $\rho e = \rho \varepsilon + \rho \boldsymbol{v}\boldsymbol{v}/2$, where e is the specific total energy and ε is the specific internal energy.

3.6. Code

The numerical simulations were performed with a modified version of the hydrodynamic code Herakles (Kifonidis et al. 2003, 2006), which is a descendant of the code Prometheus developed by Bruce Fryxell and Ewald Müller (Müller et al. 1991; Fryxell et al. 1991). The hydrodynamic equations were integrated to second order accuracy in space and time using the dimensional splitting approach of Strang (1968), the PPM reconstruction scheme (Colella & Woodward 1984), and a Riemann solver for real gases according to Colella & Glaz (1984). The evolution of the chemical species was described by a set of additional continuity equations (Plewa & Müller 1999). Source terms in the evolutionary equations due to self-gravity and nuclear burning were treated by means of operator splitting. Every source term was computed separately, and its effect was accounted for at the end of the integration step. The viscosity tensor was not taken into account explicitly, since the solution of the Euler equations with the PPM scheme corresponds to the use of a sub-grid scale model that reproduces the solution of the Navier-Stokes equations reasonably well (Sitine et al. 2000; Meakin & Arnett 2007b). Thermal transport was treated in a time-explicit fashion when integrating the evolutionary equations. Self-gravity was implemented according to Müller & Steimnetz (1995), while the gravitational potential was approximated by a one-dimensional Newtonian potential derived from the spherically averaged mass distribution. The nuclear network was solved with the semi-implicit Bader-Deufelhard method that utilizes the Richardson extrapolation approach and sub-stepping techniques (Bader & Deuflhard 1983; Press et al. 1992) allowing for long effective timesteps.

The code was vectorized and enabled the adjustment of the vector length to the memory architecture. Therefore, an optimal performance with both vector and super-scalar, cache-based machines could be achieved.

A program cycle for two-dimensional runs consisted of two hydrodynamic timesteps and proceeds as follows:

1. the hydrodynamic equations were integrated in the r-direction (r-sweep), including the effects of heat conduction. The time-averaged gravitational forces were computed, and the momentum and the total energy were updated to account for the gravitational source terms. Subsequently, the equation of state was called to update the thermodynamic state due to the change in the total energy;
2. Step (1) was repeated in θ-direction (θ-sweep);
3. the nuclear network was solved in all zones with significant nuclear burning ($T > 10^8$ K). Subsequently, the equation of state was called to update the pressure and temperature;
4. in the subsequent timestep, the order of Step (1) and (2) was reversed to guarantee second-order accuracy in the time integration, and Step (3) was repeated with the updated quantities;
5. the size of the timestep for the next cycle was determined.

For one-dimensional runs, Step (2) and Step (4) were omitted.

When using spherical coordinates, the CFL stability condition on the timestep was most restrictive near the origin of the grid. However, inside a region beneath the off-center temperature maximum, there were no significant non-radial motions to be expected during the evolution of the core helium flash except in the immediate vicinity of the temperature inversion, where convective overshooting may occur. Hence, removing the center of the computational grid did not generate any numerical bias, but conserved considerable amounts of computational time. In

Table 2. Some properties of the 1D simulations: number of radial grid points (N_r), radial resolution (Δr in 10^6 cm), time up to the thermonuclear runaway t_{trn}, and maximum evolution time t_{max} (both in s).

Run	N_r	Δr	t_{trn}	t_{max}
hefl.1d.1	180	5.55	40 700	42 500
hefl.1d.2	270	3.77	14 600	16 250
hefl.1d.3	360	2.77	12 300	15 600

the radial direction, we used a closed (i.e. reflective) outer and inner quasi-hydrostatic boundary obtained by means of polynomial extrapolation, which significantly suppressed any artificial velocity fluctuations resulting from an imbalance of gravitational and pressure forces in the boundary zones. For two-dimensional runs, the boundary conditions in the angular direction were also reflective.

After interpolation and stabilization, the initial model in the two-dimensional simulations had to be perturbed explicitly to trigger convection, because an initially exactly spherically symmetric model remains that way forever when evolved in spherical coordinates with our code. We imposed a random flow field with a maximum (absolute) velocity of 10 cm s^{-1}, and random density perturbations with $\Delta\rho/\rho \leq 10^{-2}$.

4. Results of 1D simulations

We performed several one-dimensional simulations using model M, which differed only in their grid resolution (see Table 2), in order to assess, whether a thermonuclear runaway could be avoided without a convective flow.

Figure 5 demonstrates that heat conduction and adiabatic expansion alone fail to stabilize the model, i.e. one-dimensional hydrodynamic simulations result in a thermonuclear runaway. Initially, the maximum temperature increases only slowly, but starts to rise rapidly after a time t_{trn} (Table 2) up to a value $T \sim 10^9$ K. For instance, from the temperature evolution of model hefl.1d.3, one can determine that a local hot spot with a temperature of 2.3×10^8 K will runaway after about 80 s (Fig. 6). The time at which the runaway is triggered depends on the grid resolution, being longer in models with lower resolution (Fig. 5).

In every case, a thermonuclear flame with $T \sim 10^9$ K eventually forms and propagates outwards with subsonic velocity depending on the grid resolution. Since our two-dimensional (more realistic) simulations do not show such a behavior, we refrain from further discussion of the one-dimensional simulations.

5. Results of 2D simulations

In Table 3, we summarize some characteristic parameters of our two-dimensional simulations which are based on model M.

We first discuss in some detail one specific simulation hefl.2d.3, which serves as a standard to which we compare the results of our other simulations. Thereafter, we discuss some general properties of all 2D simulations. Every simulation covered approximately 3×10^4 s (~8 h) of the evolution near the peak of the core helium flash. They were performed on an equidistant spherical grid encompassing 95% of the helium core mass (X(^{4}He) > 0.98) except for a central region with a radius of $r = 2 \times 10^8$ cm, which was removed in order to allow the use of longer timesteps. This radius is sufficiently smaller than the radius of the temperature inversion ($r \sim 5 \times 10^8$ cm) and therefore its presence does not influence the convection zone.

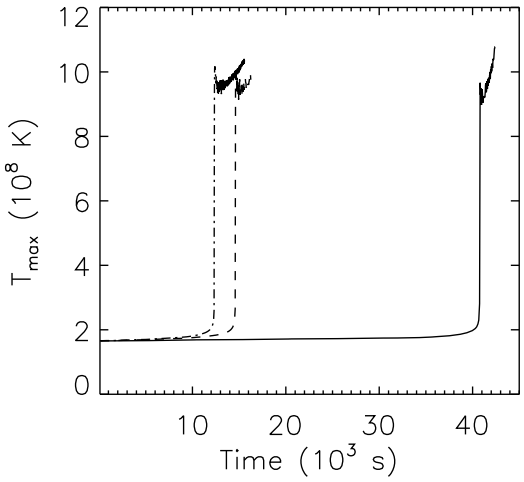

Fig. 5. Evolution of the temperature maximum T_{max} in the one-dimensional models hefl.1d.1 (solid), hefl.1d.2 (dashed), and hefl.1d.3 (dash-dotted), respectively.

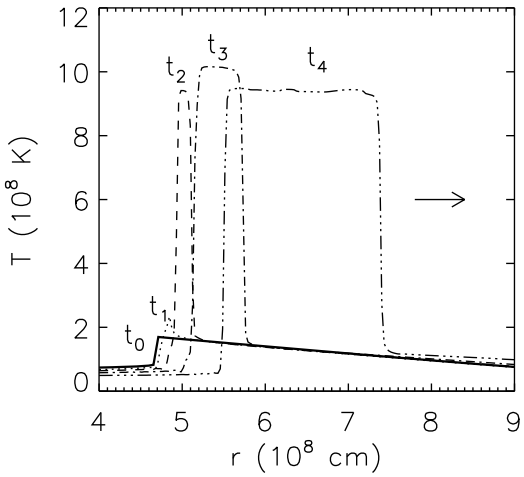

Fig. 6. Temperature stratification across the helium core in model hefl.1d.3 during the runaway at t_1 = 12 270 s (dotted), t_2 = 12 352 s (dashed), t_3 = 12 392 s (dash-dotted), and t_4 = 12 762 s (dash-dot-dotted), respectively. The solid line corresponds to the initial model (t_0), and the arrow indicates the direction of the flame propagation.

5.1. Simulation hefl.2d.3

After the beginning of the simulation, the initial velocity perturbations started to grow in a narrow layer just outside the temperature maximum ($r \sim 5 \times 10^8$ cm), i.e. in the region heated by nuclear burning. Later on at $t \sim 800$ s, several hot bubbles appeared, which rose upwards with maximum velocities of $\sim 4 \times 10^6$ cm s^{-1}. They were typically about 0.2% hotter than the angular-averaged temperature at a given radius. The ^{4}He mass fraction of all hot bubbles was about 0.4% less than the corresponding angular-averaged value, since helium was depleted in the bubbles by the triple α reaction. Consequently, ^{12}C and ^{16}O (produced in helium burning) were enhanced by ~0.7% in the bubbles.

During the first 700 s of the evolution, the off-center maximum mean temperature $\langle T \rangle_{max}$ rose at a rate of ~1000 K s^{-1}, until it reached a value $\sim 1.67 \times 10^8$ K. At this moment, from the region at the $\langle T \rangle_{max}$, the bubbles emerged and caused its decrease by $\sim 2.6 \times 10^6$ K in just 570 s corresponding to a temperature drop rate of 4540 K s^{-1} (Fig. 7). This phase marked the

Table 3. Some properties of the 2D simulations: number of grid points in radial (N_r) and angular (N_θ) direction, radial (Δr in 10^6 cm) and angular grid resolution ($\Delta\theta$), characteristic length scale l_c of the flow (in 10^8 cm), characteristic rms velocity v_c of the flow (in 10^6 cm s^{-1}) averaged over the width of the convection zone $R \sim l_c$, Reynolds number R_n associated with the numerical viscosity of our code (Porter & Woodward 1994), damping timescale due to the numerical viscosity t_n, typical convective turnover time $t_o = 2\,R/v_c$, and maximum evolution time t_{max} (in s), respectively.

Run	Grid	Δr	$\Delta\theta$	l_c	v_c	R_n	t_n	t_o	t_{max}
hefl.2d.1	180 × 90	5.55	2°	4.7	1.29	1900	11 000	730	30 000
hefl.2d.2	270 × 180	3.70	1°	4.7	1.79	8900	36 000	525	30 000
hefl.2d.3	360 × 240	2.77	0.75°	4.7	1.84	21 000	83 000	510	30 000

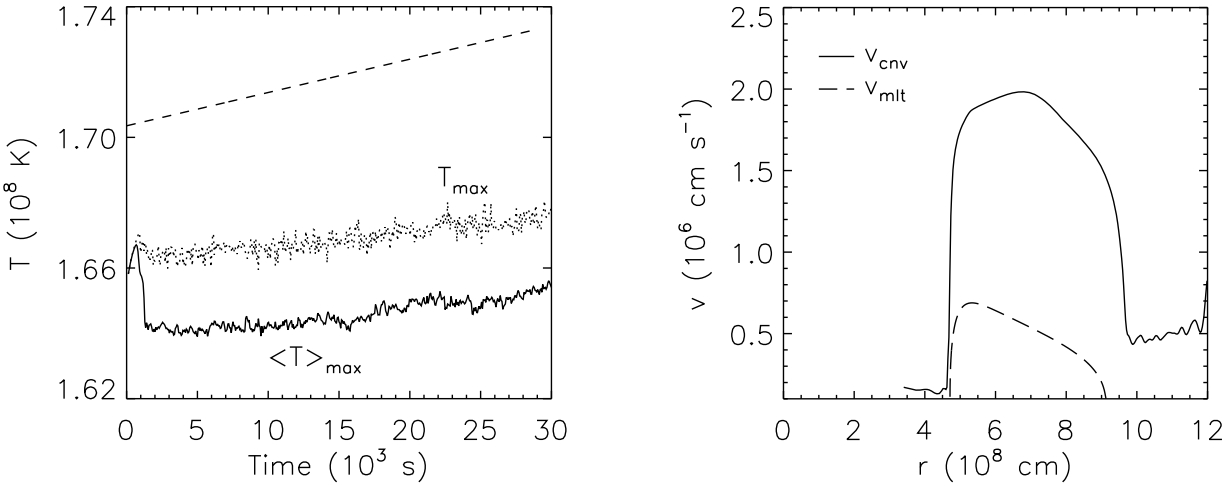

Fig. 7. *Left panel*: temporal evolution of the horizontally averaged temperature maximum $\langle T \rangle_{max}$ (solid), and the global temperature maximum T_{max} (dotted) in model hefl.2d.3. The dashed line corresponds to the temporal evolution of the maximum temperature in the stellar evolutionary calculations of model M. *Right panel*: the rms convection velocity v_{cnv} in simulation hefl.2d.3 averaged over 6000 s (solid) versus the convection velocity predicted by the mixing length theory v_{mlt} (dashed).

onset of convection (Fig. 8), where a fraction of the thermonuclear energy released via helium burning started to be transported efficiently away from the burning regions by mass flow, thereby inhibiting a thermonuclear runaway.

As soon as the bubbles had formed, they rose upwards and started to interact and merge, i.e. the convective layer began to grow in radius. About ~1300 s after the start of the simulation, the entire convection zone was covered by an almost stationary flow pattern of almost constant total kinetic energy roughly equal to 10^{45} erg. At this time, vortices dominated the flow pattern. They extended across the entire convective region (width $R \sim 3\,H_p$), and were of approximately similar angular size, one vortex covering about 40 degrees (diameter ~5×10^8 cm). Usually we found about four such vortices with two dominant up-flows of hot gas at both $\theta \sim 60°$ and $\theta \sim 120°$ (see, e.g. Fig. 8). These large vortices were rather stable, surviving until the end of our simulations. Typical convective flow velocities were $v_{cnv} \sim 1.8 \times 10^6$ cm s^{-1}, well below the local sound speed $c_S \sim 1.7 \times 10^8$ cm s^{-1}, i.e. a vortex required about 500 s for one rotation. The persistence of vortices is not typical for turbulent convection.

The dominance of the large scale structures (vortices) was a consequence of the imposed axial symmetry, which eliminated the vortex folding term in the vorticity evolution equation of the flow (Pope 2000; Meakin & Arnett 2007a).

The Mach number M of the convective flow was ~0.01. Is PPM suited for this type of subsonic flow? This question, which is beyond the scope of the present study, needs to be investigated. It is known that the artificial viscosity of standard Riemann solver methods exhibit an incorrect scaling with the flow Mach number as $M \to 0$ (Turkel 1999), i.e. the inherent artificial viscosity of PPM may be too high for simulating flows at low Mach numbers (e.g. $M \sim 0.01$) adequately.

However, Meakin & Arnett (2007a) demonstrated that the PPM method operates well even at these low Mach numbers.

Energy transport by convection within the vortices is concentrated into a few narrow upward drafts, compensated partially, but only to a small extent, by down-flows. The vortices transport energy mostly along their outer edges. Matter in their centers does not interact at all with the regions of dominant nuclear energy production.

The horizontally averaged value of the maximum temperature, barring some additional temperature fluctuations due to convection, increased slightly following the onset of convection during the entire subsequent evolution at an approximate rate 40 K s^{-1} (see Fig. 7).

This rate appears to be about 60% lower than the rate measured in the stellar evolutionary calculations (~100 K s^{-1}): this could be the result of either an initially lower value of the temperature maximum, after the stabilization phase, at the beginning of the simulation (see Sect. 2), or more dynamic convective motion, since the mean convective velocities v_{cnv} exceed the velocities predicted by mixing length theory, v_{mlt}, on average by a factor of four (Fig. 7).

Convection distributes the energy in such a way that the temperature gradient ∇ never exceeds ∇_{ad} significantly in model M. Although, the value of ∇ established at the beginning of the simulation deviates slightly after some time from the gradient at later times, it remains close to the adiabatic temperature gradient ∇_{ad} (the relative difference being less than 1%). In this respect, there is no indication of any significant deviation from the situation obtained in stellar evolutionary calculations.

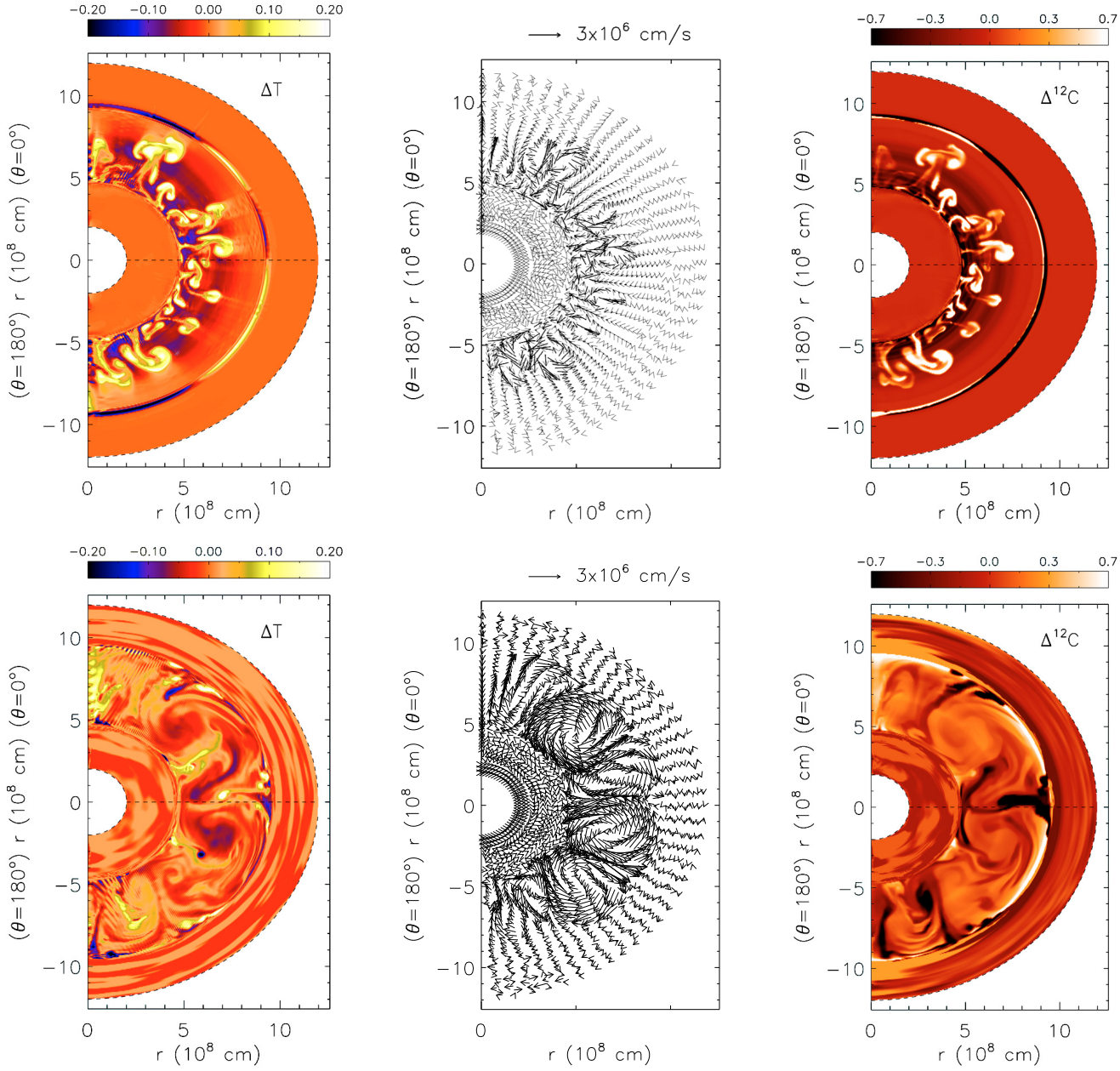

Fig. 8. Snapshots of the onset of convection at 1020 s (*upper panels*), and of the evolved convection at 29 000 s (*lower panels*) in model hefl.2d.3, showing the temperature contrast $\Delta T = 100 \times (T - \langle T \rangle_\theta)/\langle T \rangle_\theta$ (*left panels*), the velocity field (*middle panels*), and the ^{12}C contrast $\Delta^{12}\mathrm{C} = 100 \times (^{12}\mathrm{C} - \langle {}^{12}\mathrm{C} \rangle_\theta)/\langle {}^{12}\mathrm{C} \rangle_\theta$ (*right panels*), respectively. $\langle\rangle_\theta$ denotes a horizontal average at a given radius.

The apparent spike in the initial ^{12}C distribution at the location of the temperature maximum (Fig. 3) is a result of a non-instantaneous treatment of the convective mixing in stellar evolutionary calculations. It turns out that a non-instantaneous treatment of mixing is not required during the core helium flash since simulation hefl.2d.3 indicate that the spike is smeared out immediately after convection commences. This implies that the assumption of instantaneous mixing is a good approximation locally, despite the strong temperature dependence of the energy production rate.

5.1.1. Energy fluxes

Figure 9 displays the individual contributions of various energy fluxes, time-averaged over almost 12 convective turnover times (see Table 3), i.e. only the average effect of convection should be apparent. The derivation of these quantities is explained in Appendix A. All energy fluxes, F, describe the amount of energy transported per unit of time across a sphere of a given radius.

Most of the nuclear energy production in the convection zone occurs in a relatively narrow shell about the location of the temperature maximum. This energy is transported away by both convection and thermal transport due to heat conduction and radiation. The convective (or enthalpy) flux, F_C, varies from -0.2×10^{42} erg s^{-1} up to 1.6×10^{42} erg s^{-1}. The kinetic flux, F_K, reaches a value of at most 1×10^{42} erg s^{-1}, and is mostly positive in the convection zone, i.e. the motion has a predominantly upward direction. This implies that the fast, narrow, upwardly directed streams dominate over the slower and broader downward flows. The ratio of the extreme values of F_C and F_K is almost 2:1, i.e. nuclear energy is stored predominantly in the internal energy of the rising hot gas.

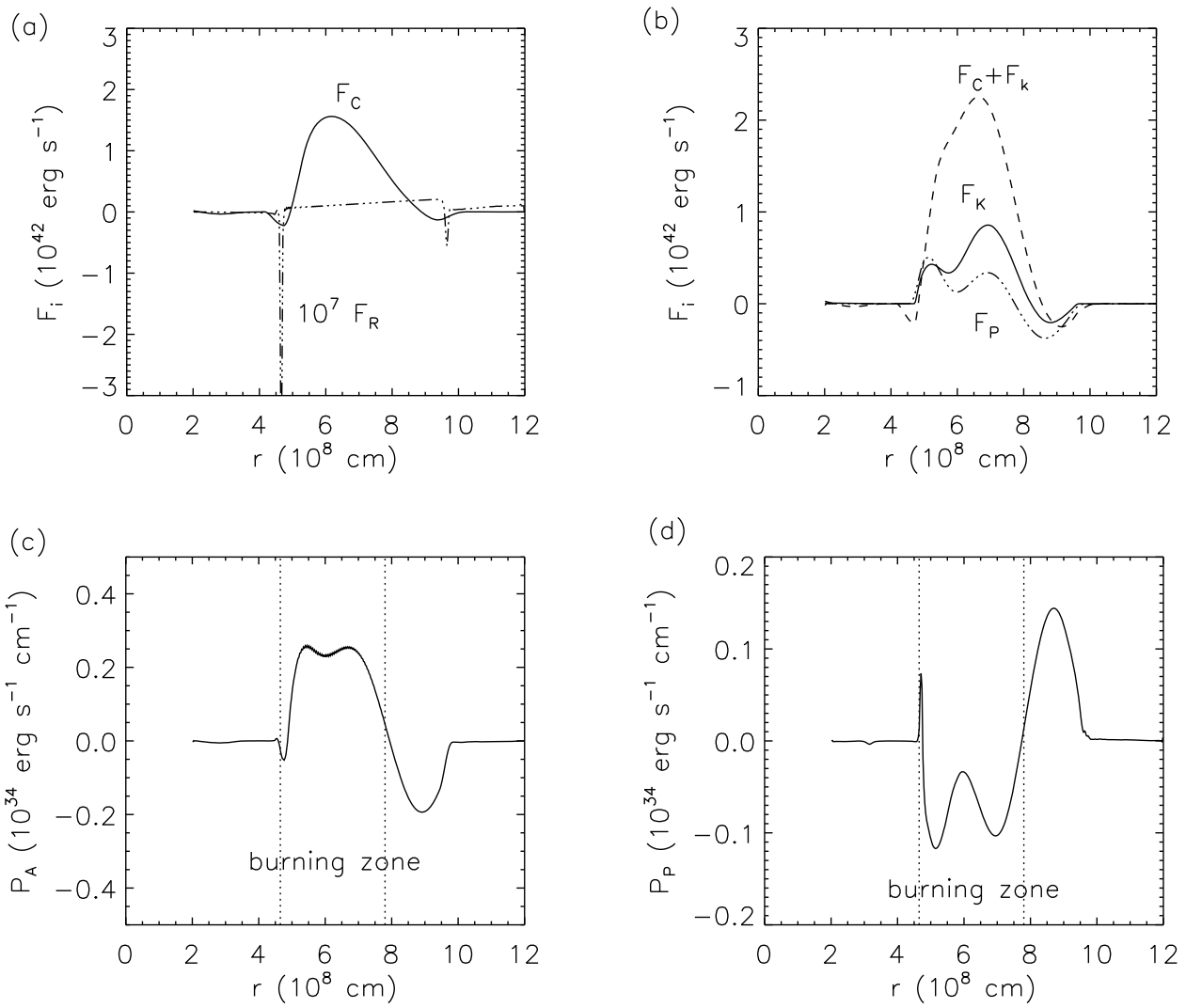

Fig. 9. Snapshots of various energy fluxes and source terms in model hefl.2d.3 (time averaged from t = 18 000 s to t = 24 000 s): **a)** convective flux F_C (solid), and the energy flux due to the thermal transport F_R (dash-dotted); **b)** kinetic flux F_K (solid), acoustic flux F_P (dash-dot-dotted), and sum of the kinetic and convective flux $F_C + F_K$ (dashed); **c)** source terms due to work done by buoyancy forces P_A, and **d)** due to volume changes P_P. The vertical lines enclose the nuclear burning zone ($T > 10^8$ K).

Both convective and kinetic energy flux transport more than 90% of the generated nuclear energy upward through the convection zone, the value is dropping to zero towards its border. Part of the heat released in the nuclear processes is in fact transported downwards towards the inner edge of the temperature inversion. Almost none of the nuclear energy reaches the surface of the helium core, either by convection or by conduction, i.e. all the energy released is deposited within the core causing its expansion. Energy transport due to heat conduction and radiation is everywhere negligible compared with other contributions. The viscous flux, F_V, is negligible as well, and losses due to friction, P_V, influence only the dynamics significantly close to the borders of the convection zone (Achatz 1995).

For completeness, we also consider the flux and source terms of the kinetic energy (see Appendix A), which allow us an additional insight into the operation of convection. The radial profile of the source term P_A, corresponding to the work done by buoyancy forces, indicates that the vertical convective flows are accelerated due to their density fluctuations in the entire region of dominant nuclear burning (burning zone) above T_{max}. Corresponding pressure fluctuations (causing expansion due to a pressure excess, respectively compression due to a pressure deficit) powered by the volume work P_P show that the gas within the burning region expands, which effectively again implies that an acceleration occurs. Due to the importance of P_P in the convection zone, the acoustic flux F_P, which transports pressure fluctuations, reaches a value comparable to that of the kinetic flux F_K, its value being negligible elsewhere.

5.1.2. Turbulent entrainment, temperature inversion and the growth of the convection zone

Turbulent entrainment (Fernando 1991; Meakin & Arnett 2007b), commonly referred to as overshooting, is a hydrodynamic process that permits mixing and heating in regions that are convectively stable according to the Schwarzschild or Ledoux criterium. Turbulent entrainment, i.e. penetration beyond the formal convective boundaries, occurs at both edges of the convection zone, and is driven by down-flows and up-flows. We study the entrainment by monitoring the temperature changes and the ^{12}C concentration at the (formal) edges of the convection zone. ^{12}C is the most suitable element for investigating the extent of

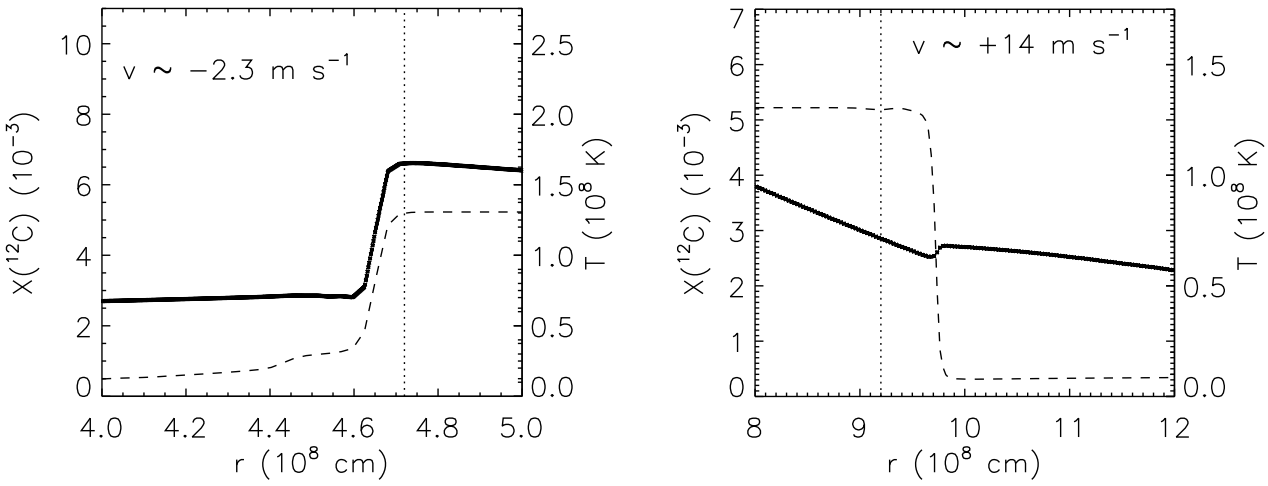

Fig. 10. Angular averaged ^{12}C distribution (dashed) and temperature stratification (thick) at the inner (*left panel*) and outer edge (*right panel*) of the convection zone in model hefl.2d.3 at $t = 30\,000$ s. The vertical dotted lines mark the initial boundaries of the convection zone at $t = 0$ s.

convective mixing, because at the beginning of the simulations, it is mostly absent outside the convection zone, and therefore can be enhanced there only due to overshooting.

At $t = 30\,000$ s, close to the end of simulation hefl.2d.3, the temperature inversion is located at $r = 4.65 \times 10^8$ cm (Fig. 10). It is therefore about 70 km closer to the center of the star than it was at the beginning of the simulation (4.72×10^8 cm). Its shape remains almost unchanged and discontinuous during the whole simulation, and its propagation speed can be estimated from the heating rate $\delta T/\delta t \sim 2760$ K s^{-1} and the local gradient $\delta T/\delta r \sim 12$ K cm^{-1} at the steepest point of the inversion:

$$v \simeq -(\delta T/\delta t)\,/\,(\delta T/\delta r) \sim -2.3 \text{ m s}^{-1}. \quad (16)$$

This speed is significantly higher than the propagation speed due to heat conduction alone. We note that the energy flux carried by the heat conduction is seven orders of magnitude smaller than the energy flux carried by the convection. Assuming that the convective energy flux at the position of the temperature inversion ($F_c \sim 0.2 \times 10^{42}$ erg s^{-1}) is used up completely to heat the layers beneath the temperature inversion, a typical heating rate of $\dot{T} = \dot{E}/C_{\rm inv} \sim 1250$ K s^{-1} can be derived, which is by roughly 50% lower than the value inferred from the simulation. $C_{\rm inv}$, the heat capacity of the layers including the temperature inversion is $\sim 1.6 \times 10^{38}$ erg K^{-1}. This implies that turbulent entrainment leads to a strong heating of the inner neutrino-cooled center of the star that occurs on timescales relatively short compared with stellar evolutionary timescales. This heating was studied by both Deupree & Cole (1983) and Cole et al. (1985), who derived qualitatively similar results. In one-dimensional stellar evolution calculations, the temperature inversion moves outwards with time.

Assuming that the estimated propagation speed of the temperature inversion remains constant, it would reach the center of the helium core and lift the electron degeneracy there within 24 days. This scenario would exclude the occurrence of mini-flashes after the main core helium flash, which are observed in stellar evolutionary calculations (Fig. 4).

Sweigart & Gross (1978) found that in stars with higher mass and helium abundance, the flash occurs closer to their center, which implies that in these stars can the temperature inversion reach the center of the helium core due to the turbulent entrainment even faster.

We also found that turbulent entrainment influenced the outer boundary of the convection zone. In the initial model, this boundary was located at $r = 9.2 \times 10^8$ cm and corresponded to a discontinuous change in the distribution of elements (Fig. 3), which is in stellar evolution models a consequence of the assumed instantaneous mixing. In these models, all species in the convectively unstable region are mixed instantaneously across the entire convection zone, while the regions that are assumed to be convectively stable do not experience any mixing at all.

The distribution of ^{12}C at the end of our simulation hefl.2d.3 is depicted in Fig. 10. Compared with that of the initial model, there is a clear shift of the carbon discontinuity, at the outer edge of the convection zone, to a larger radius ($r = 9.7 \times 10^8$ cm). In hydrodynamic simulations, the gas overshoots naturally from the convectively unstable to the formally convectively stable region because of its inertia. At the boundaries of the convection zone, the overshooting appears to destroy the stability, according to the Schwarzschild criterium, transforming the originally convectively stable region into a convectively unstable one. This allows the boundary to propagate further when a subsequent load of gas will try to overshoot at a later time. We estimated that the propagation speed of the outer boundary of the convection zone was about 14 m s^{-1}. With a propagation speed of this magnitude, the convection zone would reach the hydrogen-rich layers surrounding the helium core at a radius $r = 1.9 \times 10^9$ cm and trigger a hydrogen injection flash (Schlattl et al. 2001) within 10 days. Expected hydrodynamic phenomena due to the extra hydrogen mixing into the helium burning shell via this extended convection zone could alter the structure of the star significantly. Additional nucleosynthesis could also be triggered because hydrogen entrainment will result in a production of neutrons and possibly also to a production of some *s*-process elements.

The hydrogen injection flash in Pop I stars is in contradiction with the canonical stellar evolutionary calculations where stars fail to inject hydrogen to the helium core during the core helium flash, unless their metallicity is close to zero (Fujimoto et al. 1990).

Since the turbulent entrainment at the inner convective boundary involved just three radial grid zones in the longest simulations that we performed, the estimated propagation velocity must be interpreted with caution and be considered as an order of magnitude estimate. The turbulent entrainment at the outer convective boundary involved eighteen numerical zones in the radial direction: the estimated propagation velocity has higher confidence level.

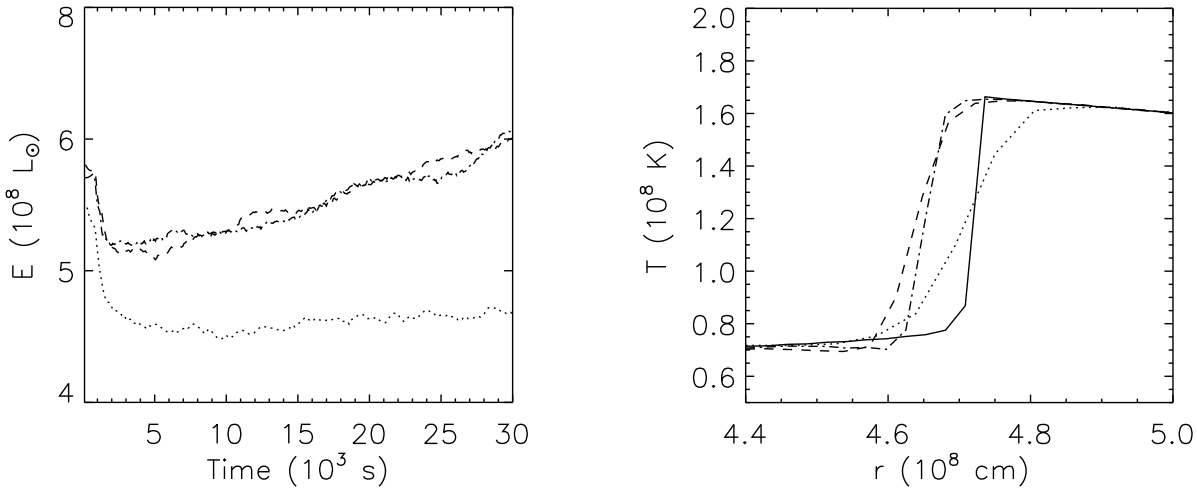

Fig. 11. *Left panel*: evolution of the total energy production rate in solar luminosity $L_\odot$ for models hefl.2d.1 (dotted), hefl.2d.2 (dashed), and hefl.2d.3 (dash-dotted), respectively. *Right panel*: mean temperature distribution near the temperature inversion for models hefl.2d.1 (dotted), hefl.2d.2 (dashed), and hefl.2d.3 (dash-dotted) at a $t = 30\,000$ s, respectively. The initial distribution is shown by the solid line.

5.1.3. Two-dimensional models with different resolution

We found only minor differences between the properties of model hefl.2d.3 and those of the corresponding models computed with a different grid resolution.

First, the initial mapping process generated different interpolation errors for different grid resolutions. However, the major source of discrepancy in this phase of the calculation was the stabilization itself. The iterative procedure that minimized the numerical fluxes across zone boundaries (to retain the model in hydrostatic equilibrium) tends to decrease the temperature stronger in models of lower resolution.

Another source of discrepancy was caused by the numerical diffusion, which was obviously stronger in models of lower resolution. Therefore, model hefl.2d.1 suffered more from numerical diffusion than either model hefl.2d.2 or hefl.2d.3, which is evident from Fig. 11. The temperature inversion, which at the beginning is almost discontinuous, is smoothed out faster in model hefl.2d.1. We note, that the temperature inversion is situated at smaller radii in models of higher resolution, since the typical flow velocities are higher in better resolved models (Table 3), i.e. the turbulent entrainment is more effective, and the temperature inversion propagates at higher speed.

Nevertheless, models hefl.2d.2 and hefl.2d.3 appear to be well resolved since differences between them are minor. The temporal evolution in their total nuclear energy production rates, for instance, are in almost perfect agreement (Fig. 11). The temperature fluctuations in the two-dimensional models are suppressed stronger in models of higher resolution. More intense temperature fluctuations observed in models which we calculated with grid resolutions even lower than that of the model hefl.2d.1, did not lead to an explosion.

6. Summary

We have presented one- and two-dimensional (i.e. axisymmetric) hydrodynamic simulations of the core helium flash close to its peak covering about eight hours of evolution time. We found no hydrodynamic events that deviated significantly from the predictions of stellar evolutionary calculations. After an initial adjustment phase the 2D models reached a quasi-steady state where the temperature and nuclear energy production rate were increasing only slowly.

Convection played a crucial role in keeping the star in hydrostatic equilibrium. Based on our two-dimensional simulation of the highest grid resolution (model hefl.2d.3), convection followed the predictions of mixing length theory approximately, although the temperature gradient of our dynamically evolved 2D models deviated slightly from that of the initial model obtained from (1D) stellar evolutionary calculations (the relative difference was lower than 1%). The maximum temperature $\langle T \rangle_{\rm max}$ in our best resolved model hefl.2d.3 rose at a rate of about 40 K s^{-1}, which was about 60% lower than the rate predicted by stellar evolutionary calculations. The mean convective velocity exceeded the velocities predicted by mixing length theory by up to factor of four.

We note here, that in general, the velocities found in two-dimensional hydrodynamical simulations tend to exceed those in their three-dimensional (3D) counterparts where the velocities tend to agree with the predictions of mixing length theory better (Meakin & Arnett 2007b).

During the early evolution ($t < 1000$ s) of our 2D simulations, the size of the convective region did not deviate from that of the initial (hydrostatic) model. However, after a stable convective pattern was established, our 2D simulations showed that the convective flow, consisting of four quasi-stationary large scale (~40 degrees angular width) vortices, started to push the inner and outer boundary of the convection zone, initially determined by the Schwarzschild stability criterium, towards the center of the star at a velocity of 2.3 m s^{-1}, and towards the stellar surface at a velocity of 14 m s^{-1}, respectively. This produced a rapid growth in the radial extent of the convection zone on dynamic timescales. The boundary velocities may depend on the grid resolution and/or on the dimensionality of the flow. Therefore, they should be considered as order of magnitude estimates only. We plan to address this issue in a forthcoming paper.

Our 2D simulations further suggested that it is unlikely that the core helium flash is followed by subsequent core helium mini-flashes, which are observed in (1D) stellar evolutionary calculations, since the inner convective boundary can reach the center of the core in less than one month. On the other hand, the injection of hydrogen from the stellar envelope into the helium core is likely to happen within 10 days, which contradicts the predictions of the canonical evolution of low-mass Pop I stars.

Since our 2D axisymmetric simulations are probably unable to capture accurately an intrinsic three-dimensional behaviour of the convective flow, we have started to develop 3D simulations of the core helium flash. In addition, we plan to extend our 2D simulations to time intervals of several days instead of hours. The results of these long-term 2D simulations and of the first well resolved 3D simulations of the core helium flash will be presented elsewhere.

Acknowledgements. The calculations were performed at the Rechenzentrum Garching on the IBM pSeries Power5 system, and at the Leibniz-Rechenzentrum of the Bavarian Academy of Sciences and Humanities on the SGI Altix 4700 system. The authors want to thank Frank Timmes for some of his public Fortran subroutines which we used in the Herakles code for calculating the core helium flash models. We also thank Kurt Achatz, whose unpublished hydrodynamic simulations of the core helium flash, performed as part of his diploma work, have motivated and inspired us. The authors are grateful to an anonymous referee for his/her comments which helped to improve this manuscript.

Appendix A: Energy fluxes

An analysis of the vertical energy transport investigates the importance of the different physical processes occurring in the convection zone. To separate the various contributions to the total energy flux (Hurlburt et al. 1986; Achatz 1995), one integrates the hydrodynamic equation of energy conservation

$$\partial_t(\rho e) + \partial_i(v_i(\rho e + p) - v_j\Sigma_{ij} - K\partial_i T) = -\rho v_i \partial_i \Phi, \quad i,j = 1,2,3 \tag{A.1}$$

(with $e = \varepsilon + v_i v_i/2$ being the specific total energy density) over angular coordinates (θ, ϕ), and separates both the specific enthalpy ($\varepsilon + p/\rho$) and the kinetic energy ($v_i v_i/2$) into a horizontal mean and a perturbation ($f \equiv \overline{f} + f'$). This results in

$$\partial_t E + \partial_r(F_\mathrm{C} + F_\mathrm{K} + F_\mathrm{R} + F_\mathrm{V} + F_\mathrm{E}) = 0 \tag{A.2}$$

with[1]

$$E = \oint \rho e\, r^2 \mathrm{d}\Omega \tag{A.3}$$

$$F_\mathrm{C} = \oint v_r \rho \cdot \left(\varepsilon + \frac{p}{\rho}\right)' r^2 \mathrm{d}\Omega \tag{A.4}$$

$$F_\mathrm{K} = \oint v_r \rho \cdot \left(\frac{1}{2} v_i v_i\right)' r^2 \mathrm{d}\Omega, \quad i = 1,2,3 \tag{A.5}$$

$$F_\mathrm{R} = -\oint K \partial_r T\, r^2 \mathrm{d}\Omega \tag{A.6}$$

$$F_\mathrm{V} = -\oint v_i \Sigma_{ri}\, r^2 \mathrm{d}\Omega, \quad i = 1,2,3 \tag{A.7}$$

$$F_\mathrm{E} = 4\pi r^2 \overline{v_r \rho} \cdot \left(\overline{\varepsilon + \frac{p}{\rho}} + \overline{\frac{1}{2} v_i v_i} + \partial_r \Phi\right). \tag{A.8}$$

The various terms F_i indicate the total energy transported per unit time across a sphere by different physical processes. They are the convective (or enthalpy) flux F_C, the flux of kinetic energy F_K, the flux by heat conduction and radiation F_R, and the viscous flux F_V. Finally, F_E collects all terms causing a spherical mass flow, i.e. the model expansion or contraction, while F_C and F_K represent the deviations from this mean energy flow (vortices). The F_C and F_K are the major contributors to the heat transport by convection, while F_V is usually negligibly small.

[1] The gravitational potential Φ was assumed to be constant for simplicity.

In a similar way, we can also formulate a conservation equation for the mean horizontal kinetic energy, which provides further insight into the effects of convective motions. Using the other hydrodynamic equations

$$\partial_t(\rho) + \partial_i(\rho v_i) = 0 \tag{A.9}$$

$$\partial_t(\rho v_i) + \partial_j(\delta_{ij} p + \rho v_i v_j - \Sigma_{ji}) = -\rho \partial_i \Phi, \tag{A.10}$$

$$i,j = 1,2,3 \tag{A.11}$$

and $\partial_t(\rho v_i v_i/2) = v_i \partial_t(\rho v_i) - v_i v_i \partial_t \rho/2$, one finds

$$\partial_t E_\mathrm{K} + \partial_r(F_\mathrm{K} + F_\mathrm{P} + F_\mathrm{V} + F_\mathrm{E,K}) = P_\mathrm{A} + P_\mathrm{P} + P_\mathrm{V} + P_\mathrm{E,K}. \tag{A.12}$$

In terms of F_K and F_V as introduced above, one obtains

$$E_\mathrm{K} = \oint \frac{\rho}{2} v_i v_i\, r^2 \mathrm{d}\Omega \tag{A.13}$$

$$F_\mathrm{P} = -\oint v_r p'\, r^2 \mathrm{d}\Omega \tag{A.14}$$

$$F_\mathrm{E,K} = 4\pi r^2 \overline{v_r \rho} \cdot \left(\overline{\frac{p}{\rho} + \frac{v_i v_i}{2}}\right) \tag{A.15}$$

$$P_\mathrm{A} = -\oint v_r \rho' \partial_r \Phi\, r^2 \mathrm{d}\Omega \tag{A.16}$$

$$P_\mathrm{P} = \oint p' \partial_i v_i\, r^2 \mathrm{d}\Omega \tag{A.17}$$

$$P_\mathrm{V} = -\oint \partial_i v_j \cdot \Sigma_{ij}\, r^2 \mathrm{d}\Omega \tag{A.18}$$

$$P_\mathrm{E,K} = 4\pi r^2 \cdot \left(\overline{p}\,\overline{\partial_i v_i} - \overline{v_r}\,\overline{\rho}\,\partial_r \Phi\right), \quad i = 1,2,3 \tag{A.19}$$

where the P_i terms are source or sink terms of the kinetic energy. They are separated into the effect of buoyancy forces (P_A), friction forces (P_V), and the work due to density fluctuations (P_P, volume changes). By analyzing the individual P_i, one can determine which process brakes or accelerates convective motion. The acoustic flux F_P, describes the vertical transport of density fluctuations. $F_\mathrm{E,K}$ and $P_\mathrm{E,K}$ describes the effect of expansion (volume work, and work against the gravitational potential), similar to F_E in Eq. (A.8).

References

Achatz, K. 1995, in Master thesis, Technical University München
Bader, G., & Deuflhard, P. 1983, Numer. Math., 41, 373
Cole, P. W., & Deupree, R. G. 1980, ApJ, 239, 284
Cole, P. W., & Deupree, R. G. 1981, ApJ, 247, 607
Cole, P. W., Demarque, P., & Deupree, R. G. 1985, ApJ, 291, 291
Colella, P., & Glaz, H. H. 1984, J. Comput. Phys., 59, 264
Colella, P., & Woodward, P. R. 1984, J. Comput. Phys., 54, 174
Cox, A. N., & Stewart, J. N. 1970a, ApJS, 19, 243
Cox, A. N., & Stewart, J. N. 1970b, ApJS, 19, 261
Dearborn, D. S. P., Lattanzio, J. C., & Eggleton, P. P. 2006, ApJ, 639, 405
Deupree, R. G. 1984a, ApJ, 282, 274
Deupree, R. G. 1984b, ApJ, 287, 268
Deupree, R. G. 1986, ApJ, 303, 649
Deupree, R. G. 1996, ApJ, 471, 377
Deupree, R. G., & Cole, P. W. 1983, ApJ, 269, 676
Deupree, R. G., & Wallace, R. K. 1987, ApJ, 317, 724
Dewitt, H. E., Graboske, H. C., & Cooper, M. S. 1973, ApJ, 181, 439
Edwards, A. C. 1969, MNRAS, 146, 445
Fernando, H. 1991, Ann. Rev. Fluid Mech., 23, 455
Fryxell, B., Arnett, D., & Müller, E. 1991, ApJ, 367, 619
Fujimoto, M. Y., Iben, I. J., & Hollowell, D. 1990, ApJ, 349, 580
Hurlburt, N. E., Toomre, J., & Massaguer, J. M. 1986, ApJ, 311, 563
Iben, Jr., I. 1975, ApJ, 196, 525
Iben, I., & Renzini, A. 1984, Phys. Rep., 105, 329

Itoh, N., Hayashi, H., Nishikawa, A., & Kohyama, Y. 1996, ApJS, 102, 411
Kifonidis, K., Plewa, T., Janka, H.-T., & Müller, E. 2003, A&A, 408, 621
Kifonidis, K., Plewa, T., Scheck, L., Janka, H.-T., & Müller, E. 2006, A&A, 453, 661
Lattanzio, J., Dearborn, D., Eggleton, P., & Dossa, D. 2006 [arXiv:astro-ph/0612147]
Meakin, C. A., & Arnett, D. 2007a, ApJ, 665, 690
Meakin, C. A., & Arnett, D. 2007b, ApJ, 667, 448
Müller, E. 1998, in Computational methods for astrophysical fluid flow, ed. O. Steiner & A. Gautschy (Berlin: Springer Verlag), Lecture Notes in Physics, 27, 343
Müller, E., & Steimnetz, M. 1995, Comp. Phys. Comm., 89, 45
Müller, E., Fryxell, B., & Arnett, D. 1991, in ESO/EIPC Workshop on Supernova 1987A and other Supernovae, 99
Plewa, T., & Müller, E. 1999, A&A, 342, 179
Pope, S. B. 2000, Turbulent flows (The Press Syndicate of the University of Cambridge)
Porter, D. H., & Woodward, P. R. 1994, ApJS, 93, 309
Potekhin, A. Y., Chabrier, G., & Yakovlev, D. G. 1997, A&A, 323, 415
Press, W. H., Tukolsky, S. A., Vetterling, W. T., & Flannery, B. P. 1992, in Numerical Recipes in FORTRAN, The Art of Scientific Computing, Second Edition (Cambridge: Cambridge University Press), 1
Rogers, F. J., Swenson, F. J., & Iglesias, C. A. 1996, ApJ, 456, 902
Schlattl, H., Cassisi, S., Salaris, M., & Weiss, A. 2001, ApJ, 559, 1082
Sitine, I. V., Porter, D. H., Woodward, P. R., Hodson, S. W., & Winkler, K.-H. 2000, J. Comput. Phys., 158, 225
Strang, G. 1968, SIAM J. Num. Anal., 5, 506
Sweigart, A. V., & Gross, P. G. 1978, ApJS, 36, 405
Thomas, H.-C. 1967, Z. Astrophys., 67, 420
Timmes, F. X., & Swesty, F. D. 2000, ApJS, 126, 501
Turkel, E. 1999, Annu. Rev. Fluid Mech., 31, 385
Villere, K. R. 1976, Ph.D. Thesis, AA, Santa Cruz, California Univ.
Weiss, A., & Schlattl, H. 2000, A&AS, 144, 487
Weiss, A., & Schlattl, H. 2007, Ap&SS, 341
Wickett, A. J. 1977, in Problems of Stellar Convection, ed. E. A. Spiegel, & J.-P. Zahn (Berlin: Springer Verlag), Lecture Notes in Physics, 71, 284
Yakovlev, D. G., & Urpin, V. A. 1980, Sov. Astron., 24, 303
Zimmermann, R. 1970, Ph.D. Thesis, University of California at Los Angeles